

## Harnessing high-dimensional hyperentanglement through a biphoton frequency comb

Zhenda Xie<sup>1,2</sup>, Tian Zhong<sup>3</sup>, Sajan Shrestha<sup>2</sup>, XinAn Xu<sup>2</sup>, Junlin Liang<sup>2</sup>, Yan-Xiao Gong<sup>4</sup>, Joshua C. Bienfang<sup>5</sup>, Alessandro Restelli<sup>5</sup>, Jeffrey H. Shapiro<sup>3</sup>, Franco N. C. Wong<sup>3</sup>, and Chee Wei Wong<sup>1,2</sup>

<sup>1</sup> *Mesoscopic Optics and Quantum Electronics Laboratory, University of California, Los Angeles, CA 90095*

<sup>2</sup> *Optical Nanostructures Laboratory, Columbia University, New York, NY 10027*

<sup>3</sup> *Research Laboratory of Electronics, Massachusetts Institute of Technology, Cambridge, MA 02139*

<sup>4</sup> *Department of Physics, Southeast University, Nanjing, 211189, People's Republic of China*

<sup>5</sup> *Joint Quantum Institute, University of Maryland and National Institute of Standards and Technology, Gaithersburg, Maryland 20899, USA*

### I. Theory of two-photon interference of the high-dimensional biphoton frequency comb

Considering the Hong-Ou-Mandel (HOM) interference at an ideal 50:50 coupler, we can write the electric field operators at the two detectors D<sub>1</sub> and D<sub>2</sub> as

$$\hat{E}_1(t) = \frac{1}{\sqrt{2}} [\hat{E}_s(t) + \hat{E}_i(t + \delta T)], \quad \hat{E}_2(t) = \frac{1}{\sqrt{2}} [\hat{E}_s(t) - \hat{E}_i(t + \delta T)], \quad (1)$$

with the field operators before the HOM interferometer  $\hat{E}_k(t)$ , ( $k = s, i$ ) given by

$$\hat{E}_k(t) = \frac{1}{\sqrt{2\pi}} \int d\omega \hat{a}_k(\omega) e^{-i\omega t}, \quad (2)$$

where  $\delta T$  is the arrival time difference for the signal and idler photons from the crystal to the coupler. Then the two-photon coincidence detection rate is expressed as

$$R_{12} \propto \int_{T_g} d\tau G_{12}^{(2)}(t, t + \tau), \quad (3)$$

with the correlation function given by

$$G_{12}^{(2)}(t, t + \tau) = \langle \psi | \hat{E}_1^\dagger(t) \hat{E}_2^\dagger(t + \tau) \hat{E}_2(t + \tau) \hat{E}_1(t) | \psi \rangle = \left| \langle 0 | \hat{E}_2(t + \tau) \hat{E}_1(t) | \psi \rangle \right|^2, \quad (4)$$

where  $T_g$  represents the timing between the detection gates. Here we assume the pump light is an ideal continuous-wave laser and thus neglect the average over the pump field. Substituting Eqs. (1), (2) and the spontaneous parametric downconverted (SPDC) state into Eq. (4) we obtain

$$G_{12}^{(2)}(t, t + \tau) \propto |g(\tau + \delta T) - g(-\tau + \delta T)|^2, \quad (5)$$

where we define  $g(t) \equiv \int \Phi(\Omega) e^{i\Omega t} d\Omega$  and  $\Phi(\Omega)$  denotes the spectrum amplitude. As  $T_g \gg T_c$ , where  $T_c$  is the biphoton correlation time. The time integral range in Eq. (3) can be extended to  $(-\infty, +\infty)$ . Then after the time integral we obtain the coincidence rate

$$\begin{aligned} R_{12} &\propto 1 - \text{Re} \left[ \int g^*(\tau) g(\tau + \delta T) d\tau \right] / \int |g(\tau)|^2 d\tau \\ &\propto 1 - \text{Re} \left[ \int \Phi(-\Omega) \Phi(\Omega) e^{2i\Omega \delta T} d\Omega \right] / \int |\Phi(\Omega)|^2 d\Omega \end{aligned} \quad (6)$$

For our source, the spectrum amplitude  $\Phi(\Omega)$  has the following form

$$\Phi(\Omega) = \sum_{m=-N}^N f'(\Omega) h(\Omega) f(\Omega - m\Delta\Omega) = \sum_{m=-N}^N \frac{\text{rect}(\Omega / B) \text{sinc}(A\Omega)}{(\Delta\omega)^2 + (\Omega - m\Delta\Omega)^2}, \quad (7)$$

where  $f'(\Omega) = \text{sinc}(A\Omega)$  is the phase matching spectrum function, with the full width at half

maximum (FWHM) as  $2.78 / A$ , and  $h(\Omega) = \text{rect}(\Omega / B) = \begin{cases} 1, & |\Omega / B| \leq 1/2 \\ 0, & |\Omega / B| > 1/2 \end{cases}$  is the rectangular

spectrum function resulting from the FBG, with  $B$  denoting the width. The fiber Fabry-Perot cavity (FFPC) has a Lorentzian spectrum bin function characterized by:

$f(\Omega) = f_s(\Omega) f_i(\Omega) = 1/[(\Delta\omega + i\Omega)(\Delta\omega - i\Omega)] = 1/[(\Delta\omega)^2 + \Omega^2]$ , where  $\Delta\Omega$  is the spacing between

the frequency bins and  $2\Delta\omega$  denotes the FWHM of each frequency bin. Corresponding to our measurements, we evaluate our theory using the following parameter values:  $A = 2.78 / (2\pi \times$

245 GHz) = 1.81 ps,  $B = 2\pi \times 346$  GHz =  $2.2 \times 10^{12}$  rad/s,  $\Delta\Omega = 2\pi \times 15.15$  GHz =  $95.2 \times 10^{10}$  rad/s, and  $\Delta\omega = 2\pi \times 1.36$  GHz / 2 =  $4.27 \times 10^9$  rad/s. The spectrum density  $|\Phi(\Omega)|^2$  can be described by

$$|\Phi(\Omega)|^2 = \sum_{m=-N}^N |f'(\Omega)|^2 |h(\Omega)|^2 |f(\Omega - m\Delta\Omega)|^2 = \sum_{m=-N}^N \frac{\text{sinc}^2(A\Omega) \text{rect}(\Omega/B)}{[(\Delta\omega)^2 + (\Omega - m\Delta\Omega)^2]^2}, \quad (8)$$

where we have neglected the overlaps among the frequency bins since  $\Delta\Omega \gg 2\Delta\omega$ . Moreover, as the FWHM of  $|f'(\Omega)|^2$ ,  $2.78/A$  is much larger than  $2\Delta\omega$  and the width of  $|h(\Omega)|^2$ , and  $B \gg 2\Delta\omega$ , we can make the following approximation

$$\begin{aligned} |\Phi(\Omega)|^2 &\cong \sum_{m=-N}^N |f'(Am\Delta\Omega)|^2 |h(m\Delta\Omega)|^2 |f(\Omega - m\Delta\Omega)|^2 \\ &= \sum_{m=-N}^N \frac{\text{sinc}^2(Am\Delta\Omega) \text{rect}(m\Delta\Omega/B)}{[(\Delta\omega)^2 + (\Omega - m\Delta\Omega)^2]^2} = \sum_{m=-N_0}^{N_0} \frac{\text{sinc}^2(Am\Delta\Omega)}{[(\Delta\omega)^2 + (\Omega - m\Delta\Omega)^2]^2}, \end{aligned} \quad (9)$$

where  $N_0 = \lfloor B/(2\Delta\Omega) \rfloor = 11$  is the integer part of  $B/2\Delta\Omega$ . Thus we can obtain

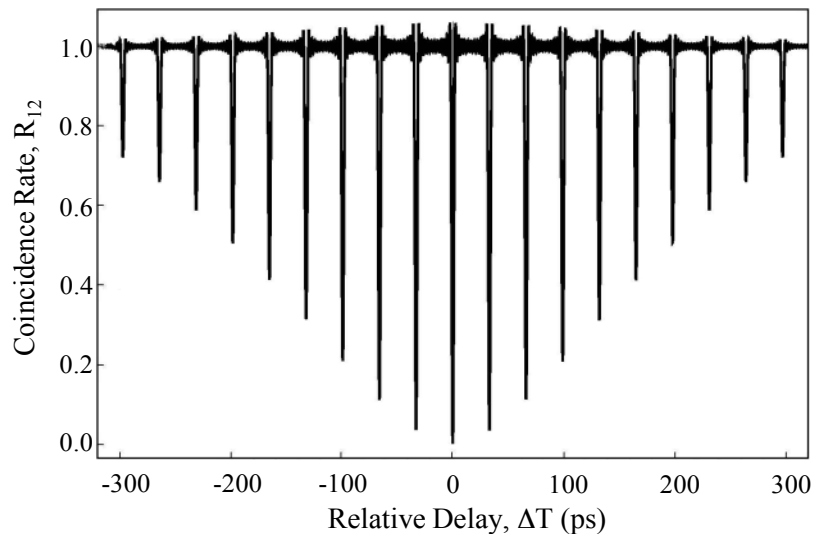
$$\int |\Phi(\Omega)|^2 d\Omega = \sum_{m=-N_0}^{N_0} \int d\Omega \frac{\text{sinc}^2(Am\Delta\Omega)}{[(\Delta\omega)^2 + (\Omega - m\Delta\Omega)^2]^2} = \frac{\pi}{2(\Delta\omega)^3} \sum_{m=-N_0}^{N_0} \text{sinc}^2(Am\Delta\Omega). \quad (10)$$

$$\begin{aligned} \int \Phi(-\Omega)\Phi(\Omega)e^{2i\Omega\delta T} d\Omega &= \int |\Phi(\Omega)|^2 e^{2i\Omega\delta T} d\Omega \\ &= \sum_{m=-N_0}^{N_0} \int d\Omega \frac{\text{sinc}^2(Am\Delta\Omega)}{[(\Delta\omega)^2 + (\Omega - m\Delta\Omega)^2]^2} e^{2i\Omega\delta T} \\ &= \frac{\pi e^{-2\Delta\omega|\delta T|} (1 + 2\Delta\omega|\delta T|)}{2(\Delta\omega)^3} \sum_{m=-N_0}^{N_0} \text{sinc}^2(Am\Delta\Omega) e^{2im\Delta\Omega\delta T} \\ &= \frac{\pi e^{-2\Delta\omega|\delta T|} (1 + 2\Delta\omega|\delta T|)}{2(\Delta\omega)^3} \left[ 2 \sum_{m=1}^{N_0} \text{sinc}^2(Am\Delta\Omega) \cos(2m\Delta\Omega\delta T) + 1 \right]. \end{aligned} \quad (11)$$

Then through Eq. (6) we arrive at the coincidence rate as

$$R_{12} \propto 1 - \frac{e^{-2\Delta\omega|\delta T|} (1 + 2\Delta\omega|\delta T|)}{\sum_{m=-N_0}^{N_0} \text{sinc}^2(Am\Delta\Omega)} \left[ 2 \sum_{m=1}^{N_0} \text{sinc}^2(Am\Delta\Omega) \cos(2m\Delta\Omega\delta T) + 1 \right]. \quad (12)$$

We model the second-order correlation based on our experimental parameters. The coincidence rate versus  $\delta T$  in the range of  $\{-320 \text{ ps}, 320 \text{ ps}\}$  is plotted in Supplementary Figure S1. We can see the interference fringe is a multi-dip pattern, with the dip revival period of about 33.2 ps, matching the 33.4 ps in our measurements. The linewidth of each Hong-Ou-Mandel dip and the fall-off in visibility for increasing  $\pm k$  bins from the zero delay point also matches with the experimental observations.



**Supplementary Figure S1 | Modeling of Hong-Ou-Mandel interference revivals for the high-dimensional biphoton frequency comb.** The coincidence counting rate  $R_{12}$  as a function of  $\delta T$ , the arrival time difference between the signal and idler photons. The fall-off in the revived visibility away from the zero delay point arises from the Lorentzian lineshape of the SPDC individual photons after passing through the cavity.

In the experiment, the bandwidth of FBG is more than that of the phase matching. It is reasonable to assume an infinite number of frequency bins, i.e.,  $N \rightarrow \infty$ , and making the replacement of  $\delta T = \delta T' + kT/2$ , where  $T = 2\pi/\Delta\Omega$ ,  $-A < \delta T' \leq T/2 - A$ , and  $k$  is an integer number, we can simplify Eq. (12) to

$$R_{12}(\delta T' + kT/2) \propto \begin{cases} 1 - e^{-2\Delta\omega|\delta T' + k\pi/\Delta\Omega|} (1 + 2\Delta\omega|\delta T' + k\pi/\Delta\Omega|)(1 - |\delta T'|/A) & -A < \delta T' < A, \\ 0 & A \leq \delta T' \leq \pi/\Delta\Omega - A. \end{cases} \quad (13)$$

We can see the dip revival period is  $T_r = \pi/\Delta\Omega \approx 33.2$  ps (or  $T/2$ ) and the visibility of the  $k$ -th order dip is  $e^{-2|k|\pi\Delta\omega/\Delta\Omega} (1 + 2|k|\pi\Delta\omega/\Delta\Omega)$ . We note that the recurrence is at  $T/2$  instead of at  $T$  in our prior analysis where the beamsplitter was moved [J. H. Shapiro, *Technical Digest of Topical Conference on Nonlinear Optics*, p.44, FC7-1, Optical Society of America (2002)]. With the beamsplitter shift, the transmitted signal and idler beams do not experience an advance or a delay, but one reflected beam is advanced while the other is delayed. In our case, only the idler beam is delayed, giving rise to the  $T/2$  recurrence in the coincidences as detailed above.

## II. Theory of Franson interference of the high-dimensional biphoton frequency comb

The electric field operators at the two detectors  $D_1$  and  $D_2$  can be expressed as

$$\hat{E}_1(t) = \frac{1}{2} [\hat{E}_s(t) + \hat{E}_s(t - \Delta T_1)], \quad \hat{E}_2(t) = \frac{1}{2} [\hat{E}_i(t) + \hat{E}_i(t - \Delta T_2)], \quad (14)$$

with the field detectors before the Franson interferometer  $\hat{E}_k(t)$ , ( $k = s, i$ ) given by

$$\hat{E}_k(t) = \frac{1}{\sqrt{2\pi}} \int d\omega \hat{a}_k(\omega) e^{-i\omega t}, \quad (15)$$

where  $\Delta T_1, \Delta T_2$  are the unbalanced arm differences. Then the two-photon coincidence detection rate can be described by

$$R_{12} \propto \int_{T_g} d\tau G_{12}^{(2)}(t, t + \tau), \quad (16)$$

with the correlation function given by

$$G_{12}^{(2)}(t, t + \tau) = \langle \psi | \hat{E}_1^\dagger(t) \hat{E}_2^\dagger(t + \tau) \hat{E}_2(t + \tau) \hat{E}_1(t) | \psi \rangle = \left| \langle 0 | \hat{E}_2(t + \tau) \hat{E}_1(t) | \psi \rangle \right|^2, \quad (17)$$

where  $T_g$  represent the timing between the detection gates. Here we assume the pump light is an ideal continuous-wave laser and thus neglect the average over the pump field. Substituting Eqs. (1), (2) and the SPDC state into Eq. (4), we obtain

$$G_{12}^{(2)}(t, t + \tau) = |G(t, t) + G(t - \Delta T_1, t - \Delta T_2) + G(t - \Delta T_1, t) + G(t, t - \Delta T_2)|^2, \quad (18)$$

with

$$G(t_1, t_2) = \frac{1}{8\pi} e^{-i\omega_p(t_1+t_2+\tau)/2} \int \Phi(\Omega) e^{i\Omega(t_2-t_1+\tau)} d\Omega = \frac{1}{8\pi} e^{-i\omega_p(t_1+t_2+\tau)/2} g(t_2 - t_1 + \tau), \quad (19)$$

where  $\Phi(\Omega)$  denotes the spectrum amplitude and we define  $g(t) \equiv \int \Phi(\Omega) e^{i\Omega t} d\Omega$ . Then we may rewrite Eq. (5) as

$$G_{12}^{(2)}(t, t + \tau) \propto \left| e^{-i\omega_p\tau/2} g(\tau) + e^{-i\omega_p(\tau-\Delta T_1-\Delta T_2)/2} g(\tau + \Delta T_1 - \Delta T_2) + e^{-i\omega_p(\tau-\Delta T_1)/2} g(\tau + \Delta T_1) + e^{-i\omega_p(\tau-\Delta T_2)/2} g(\tau - \Delta T_2) \right|^2. \quad (20)$$

As we have noted,  $\Delta T_1, \Delta T_2$  are much larger than the single-photon coherence time  $T_c$ , i.e., the range of the function  $g(t)$ , so there is only one non-zero cross term in Eq. (20). Thus we obtain

$$G_{12}^{(2)}(t, t + \tau) \propto |g(\tau)|^2 + |g(\tau + \Delta T_1 - \Delta T_2)|^2 + |g(\tau + \Delta T_1)|^2 + |g(\tau - \Delta T_2)|^2 + 2 \operatorname{Re}[e^{i\omega_p(\Delta T_1+\Delta T_2)/2} g^*(\tau) g(\tau + \Delta T_1 - \Delta T_2)]. \quad (21)$$

Since  $\Delta T_1, \Delta T_2 \gg T_g$ , the coincidence detection system can resolve the short and long paths and thus the two terms  $|g(\tau + \Delta T_1)|^2, |g(\tau - \Delta T_2)|^2$  have no contribution to the coincidence rate. Moreover, as  $T_g \gg T_c$ , the time integral range in Eq. (3) can be extended as  $(-\infty, +\infty)$ . Then after the time integral we obtain the coincidence rate

$$R_{12} \propto 1 + |\Gamma(\Delta T)| \cos[[\omega_p \Delta T / 2 + \omega_p \Delta T_2 + \varphi], \quad (22)$$

where  $\Delta T = \Delta T_1 - \Delta T_2$ , and

$$\begin{aligned} \Gamma(\Delta T) &= \int g^*(\tau) g(\tau + \Delta T) d\tau / \int |g(\tau)|^2 d\tau \\ &= \int \Phi(-\Omega) \Phi(\Omega) e^{i\Omega \Delta T} d\Omega / \int |\Phi(\Omega)|^2 d\Omega = |\Gamma(\Delta T)| e^{i\varphi}. \end{aligned} \quad (23)$$

For our source, the spectrum amplitude  $\Phi(\Omega)$  has the following form

$$\Phi(\Omega) = \sum_{m=-N}^N f'(\Omega)h(\Omega)f(\Omega - m\Delta\Omega) = \sum_{m=-N}^N \frac{\text{rect}(\Omega / B)\text{sinc}(A\Omega)}{(\Delta\omega)^2 + (\Omega - m\Delta\Omega)^2} \quad (24)$$

Then we can write the spectrum density  $|\Phi(\Omega)|^2$  as

$$|\Phi(\Omega)|^2 = \sum_{m=-N}^N |f'(\Omega)|^2 |h(\Omega)|^2 |f(\Omega - m\Delta\Omega)|^2 = \sum_{m=-N}^N \frac{\text{sinc}^2(A\Omega)\text{rect}(\Omega / B)}{[(\Delta\omega)^2 + (\Omega - m\Delta\Omega)^2]^2}, \quad (25)$$

where we have neglected the overlaps among the frequency bins since  $\Delta\Omega \gg 2\Delta\omega$ . Moreover, as the FWHM of  $|f'(\Omega)|^2$ ,  $2.78 / A \gg 2\Delta\omega$ , and the width of  $|h(\Omega)|^2$ ,  $B \gg 2\Delta\omega$ , we can make the following approximation

$$\begin{aligned} |\Phi(\Omega)|^2 &\cong \sum_{m=-N}^N |f'(Am\Delta\Omega)|^2 |h(m\Delta\Omega)|^2 |f(\Omega - m\Delta\Omega)|^2 \\ &= \sum_{m=-N}^N \frac{\text{sinc}^2(Am\Delta\Omega)\text{rect}(m\Delta\Omega / B)}{[(\Delta\omega)^2 + (\Omega - m\Delta\Omega)^2]^2} = \sum_{m=-N_0}^{N_0} \frac{\text{sinc}^2(Am\Delta\Omega)}{[(\Delta\omega)^2 + (\Omega - m\Delta\Omega)^2]^2}, \end{aligned} \quad (26)$$

where  $N_0 = \lfloor B / (2\Delta\Omega) \rfloor = 11$  is the integer part of  $B / (2\Delta\Omega)$ . Thus we can obtain

$$\int |\Phi(\Omega)|^2 d\Omega = \sum_{m=-N_0}^{N_0} \int d\Omega \frac{\text{sinc}^2(Am\Delta\Omega)}{[(\Delta\omega)^2 + (\Omega - m\Delta\Omega)^2]^2} = \frac{\pi}{2(\Delta\omega)^3} \sum_{m=-N_0}^{N_0} \text{sinc}^2(Am\Delta\Omega). \quad (27)$$

$$\begin{aligned} \int \Phi(-\Omega)\Phi(\Omega)e^{i\Omega\Delta T} d\Omega &= \int |\Phi(\Omega)|^2 e^{i\Omega\Delta T} d\Omega \\ &= \sum_{m=-N_0}^{N_0} \int d\Omega \frac{\text{sinc}^2(Am\Delta\Omega)}{[(\Delta\omega)^2 + (\Omega - m\Delta\Omega)^2]^2} e^{i\Omega\Delta T} \\ &= \frac{\pi e^{-\Delta\omega|\Delta T|} (1 + \Delta\omega |\Delta T|)}{2(\Delta\omega)^3} \sum_{m=-N_0}^{N_0} \text{sinc}^2(Am\Delta\Omega) e^{im\Delta\Omega\Delta T} \\ &= \frac{\pi e^{-\Delta\omega|\Delta T|} (1 + \Delta\omega |\Delta T|)}{2(\Delta\omega)^3} \left[ 2 \sum_{m=1}^{N_0} \text{sinc}^2(Am\Delta\Omega) \cos(m\Delta\Omega\Delta T) + 1 \right]. \end{aligned} \quad (28)$$

Then through Eqs. (6) and (10), we can write the coincidence rate as

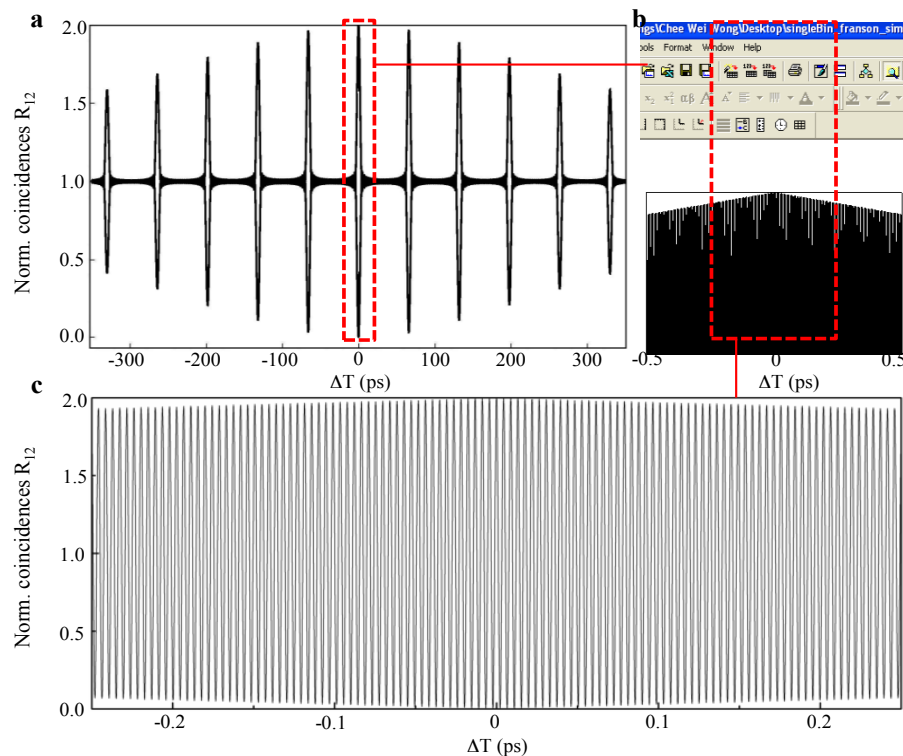
$$\begin{aligned} R_{12} &\propto 1 + \frac{e^{-\Delta\omega|\Delta T|} (1 + \Delta\omega |\Delta T|)}{\sum_{m=-N_0}^{N_0} \text{sinc}^2(Am\Delta\Omega)} \left[ 2 \sum_{m=1}^{N_0} \text{sinc}^2(Am\Delta\Omega) \cos(m\Delta\Omega\Delta T) + 1 \right] \\ &\quad \times \cos[\omega_p (\Delta T / 2 + \Delta T_2)]. \end{aligned} \quad (29)$$

Since  $\omega_p/2 = \pi c/\lambda_p = 1.43 \times 10^{12}$  rad/s  $\gg \Delta\omega, \Delta\Omega$ , the term  $\cos[\omega_p(\Delta T/2 + \Delta T_2)]$  is the fast collision part of the interference fringe with the other part determining the fringe envelope. We can simulate our experimental results with the theoretical parameters above and for  $\Delta T_2 = 5$  ns.

If we consider a large number of frequency bins such as in our measurements, i.e.,  $N \rightarrow \infty$ , and make the replacement of  $\Delta T = \Delta T' + kT$ , where  $-2A < \Delta T' \leq T - 2A$ , and  $k$  is an integer number, we can simplify Eq. (16) to

$$R_{12}(\Delta T' + kT) \propto \begin{cases} 1 + e^{-\Delta\omega|\Delta T' + 2k\pi/\Delta\Omega|} (1 + \Delta\omega|\Delta T' + 2k\pi/\Delta\Omega|) [1 - |\Delta T'|/(2A)] & -2A < \Delta T' < 2A, \\ \times \cos[\omega_p(\Delta T'/2 + k\pi/\Delta\Omega + \Delta T_2)] & \\ 0 & 2A \leq \Delta T' \leq 2\pi/\Delta\Omega - 2A. \end{cases} \quad (30)$$

The fringe envelope of the coincidence rate versus  $\Delta T$  is plotted in Supplementary Figure S2. We see that the interference fringe has a recurrent envelope that falls off away from the zero delay point due to the Lorentzian lineshape of the FFPC. The recurrence period  $T$  is about 66 ps and agrees well with repetition time of the biphoton frequency comb, i.e., the round trip time of the FFPC. The maximum visibility at the  $k$ -th order peaks can be found to be  $e^{-2|k|\pi\Delta\omega/\Delta\Omega} (1 + 2|k|\pi\Delta\omega/\Delta\Omega)$ . This gives an envelope visibility which matches well with the experimental measurements.

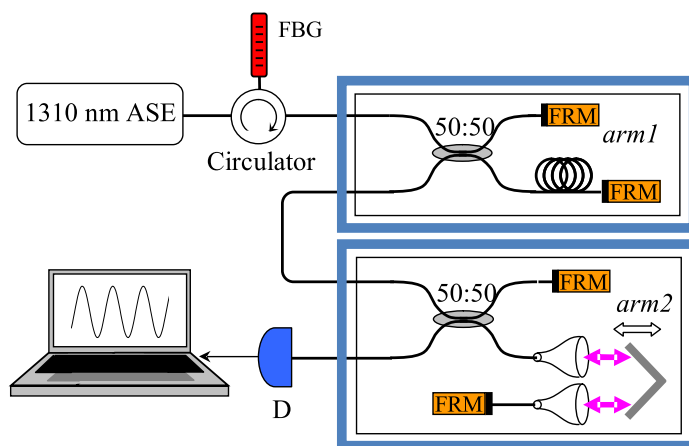


**Supplementary Figure S2 | Theory of Franson interference revival for the high-dimensional biphoton frequency comb.** **a**, The envelope of coincidence counting rates  $R_{12}$  plotted as a function of  $\Delta T$ . The interference has a recurrent envelope that falls off away from the zero delay point, arising from the finite coherence time of the single frequency bin. **b**, zoom-in of Franson interferences for the first time bin. **c**, Further zoom-in of the Franson interferences for the first time bin. The high-frequency interference oscillations arise from the phase.

### III. Characterization of Franson interferometer long-term stability

In our measurement, the fiber-based Franson interferometer needs to be stabilized at the wavelength level over long term for the phase sensitive interference measurements. All components are fixed on the aluminum housing with thermal conductive epoxy for good thermal contact. Both interferometer arms are temperature-controlled with Peltier modules and sealed in aluminum enclosures which themselves are also temperature stabilized. The delay line in *arm2* is based on a miniaturized linear stage with closed-loop piezoelectric motor control (CONEX-AG-

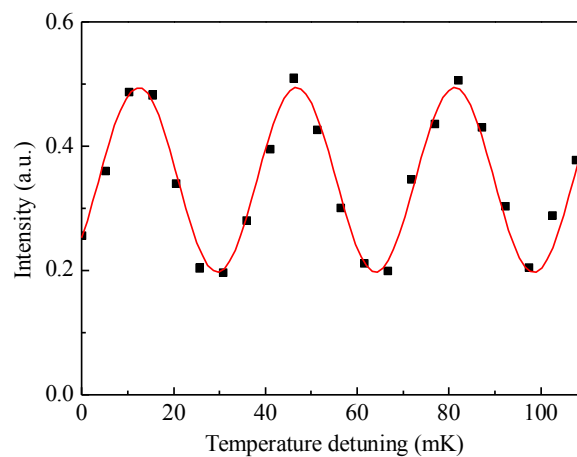
LS25-27P, Newport Corporation). The two fiber collimators are custom-built in-house with fine focal adjustment for optimized pair performance and epoxied on the housing. The delay line is aligned so that the double-pass insertion loss is less than  $0.4 \pm 0.05$  dB throughout the whole travel range of 27 mm of the linear stage. The effective delay range is about 0 to 360 ps for the reflected light, considering the double-pass optical path configuration and reflector setup.



**Supplementary Figure S3 | Long-term stability test of the Franson interferometer.** *Arm1* and *arm2* are connected in series for the classical interference test. Both interferometers are double temperature controlled, and the delay line in *arm2* is closed-loop piezoelectrically controlled. Dual collimators are custom-built in-house with fine focal adjustment and optimized performance. Fine-tuned alignment is such that the double-pass insertion loss is less than 0.4 dB throughout the whole 27 mm travel range and up to 360 ps optical delay.

We have verified the stability of the Franson interferometer using classical interference before the quantum correlation measurements. The setup is shown in Supplementary Figure S3. The light is from a 1310 nm amplified spontaneous emission (ASE) source (S5FC1021S, Thorlabs Inc.), and filtered with the same filter sub-assembly that is used in the biphoton frequency comb generation. The two arms are connected in series so that classical interference occurs between the events of passing long path of *arm1*, short path of *arm2*, and short path of *arm1*, long path of *arm2*, while  $\Delta T_1 = \Delta T_2$ . The visibility of this interference is limited to 50%,

because of other events that contribute to the background. The intensity of the output is measured using a photodiode (PDA20CS, Thorlabs Inc.), while tuning the temperature of *arm1*. The result is shown in Supplementary Figure S4. The observed interferences agree well with a sinusoidal fit, and the visibility is  $49.8 \pm 1.0\%$ , near or right at the classical limit over long measurement time periods. This indicates the Franson interferometer is well stabilized. We can also obtain the delay coefficient for this temperature tuning, which is observed to be 127 attoseconds per mK based on the fringe period when the temperature is tuned.

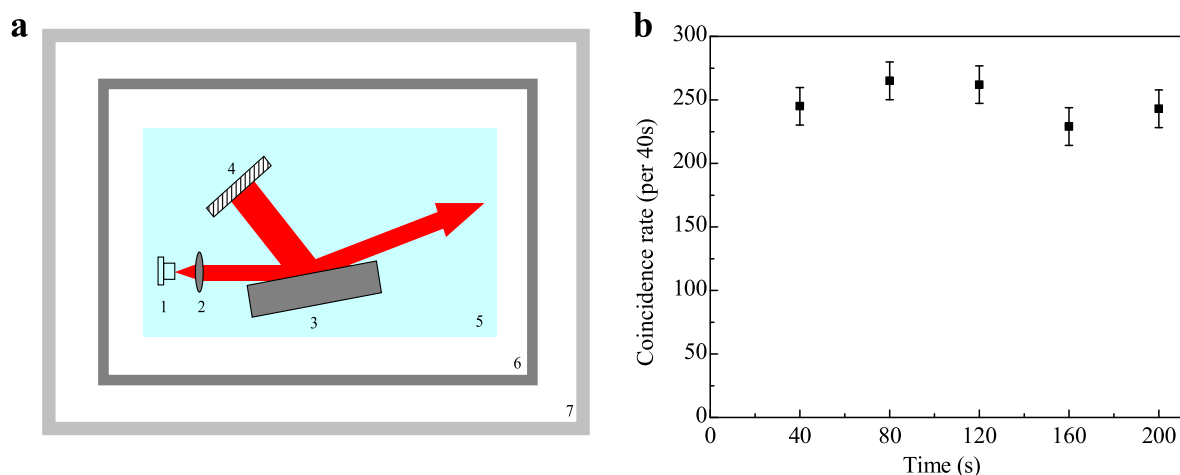


**Supplementary Figure S4 | Classical interference visibility of the stabilized coupled interferometers.** Temperature of *arm1* is tuned and the input is a 1310 nm ASE source. The temperature-delay sensitivity is observed to be 127 attoseconds per mK.

#### IV. Stabilization of the pump laser in Franson interference

The Franson interference requires high stability – both short and long term – of the pump laser, which defines the two-photon coherence time of the two-photon state. The coherence time of the pump laser should be much longer than the path length difference. This path length difference is 5 ns in our experiment. Therefore, we custom-built a stabilized laser at 658 nm using self-injection-locking. The setup is shown in Supplementary Figure S5a, which is similar to a Littman–Metcalf configuration external diode laser. The laser source that we use is a standard Fabry-Perot laser diode with center wavelength around 658 nm (QLD-658-20S). It is spatially single-mode, but has multiple longitudinal modes without feedback. A diffraction

grating is used for the longitudinal mode selection. The laser beam is first collimated onto the grating. The first-order diffraction reflects off a tunable mirror back into the diode through the grating. The zeroth order diffraction from the grating is used as the output. Because of the grating, we succeed in achieving single-mode lasing, with a mode-rejection ratio over 30 dB. The whole setup is isolated with double enclosures. The inner enclosure is made from aluminum and temperature-stabilized. The outer laser housing is also a solid piece of aluminum that is temperature-stabilized. A third temperature stabilization is applied to the diode.



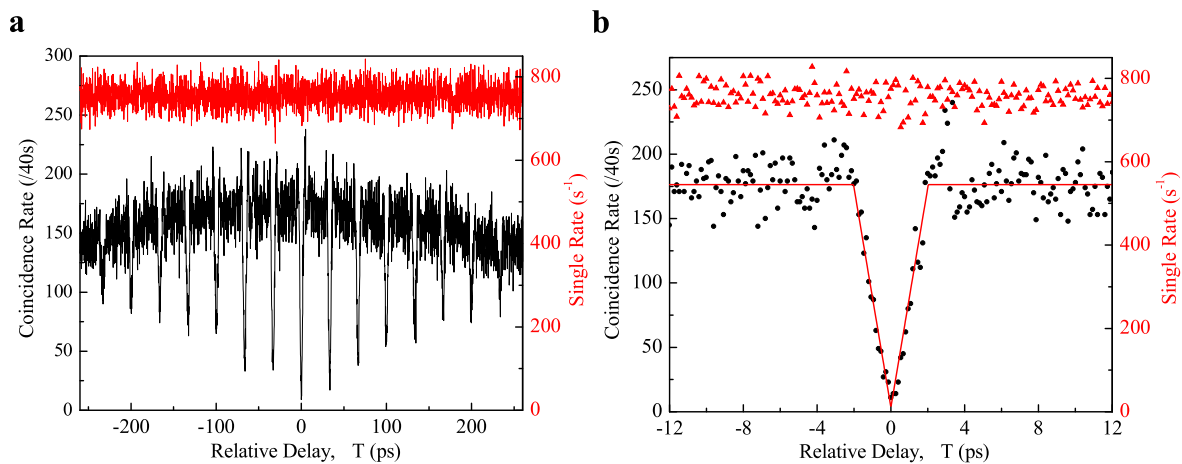
**Supplementary Figure S5 | Stabilized 658 nm pump laser with self-injection locking and characterization through Franson-type interferometer. a**, Layout schematic of custom-built 658 nm stabilized laser. 1, 658 nm Fabry-Perot laser diode with temperature stabilization; 2, collimating lens; 3, diffraction grating; 4, high-reflection mirror; 5, temperature-stabilized laser housing; 6, internal enclosure with temperature stabilization; 7, external enclosure. **b**, Franson interference measurement to demonstrate pump laser stability, with the interferometer tuned to the 0th time bin. Measurement is made at 6 mW pump power. The measured deviation of the counting rate is about 5%, with the coincidence measurements taken every 40 seconds, which corresponds to a 2 MHz drift of the pump laser. The long term drift, over 12 hours, is less than 100 MHz.

The current source for the diode is a low-noise laser diode controller (D2-105, Vescent Photonics, Inc.). With these stabilizations, we achieve a free-running wavelength drift of the 658 nm laser at less than 2 MHz within 200 seconds, which is an integration time step for the Franson measurement. The laser linewidth is measured classically with the Franson-type interferometer setup. The pump power is about 6 mW in the measurement. We tune the interferometer to the 0th time bin.  $\Delta T$  is set such that the coincidence counting rate is about the middle of the sinusoidal fringe, which gives the best sensitivity to the pump drift. The coincidence counting rate is taken every 40 seconds, and the result is shown in Supplementary Figure S5b. The measured deviation of counting rate is about 5%, which corresponds to a pump drift of 2 MHz. The long-term drift is less than 100 MHz within 12 hours (measured with a wavelength meter, HighFinesse WS-7).

## V. Measurements of Hong-Ou-Mandel revival of the high-dimensional biphoton frequency comb

In the main text, we used an InGaAs/InP single-photon detector  $D_2$  with  $\sim 2.5$  ns effective gate width for the measurements, so that the detection gate widths of  $D_1$  and  $D_2$  are always well-overlapped through the scanning range of relative delay.

Figure S6 illustrates another example of the Hong-Ou-Mandel revival when using an effective detector gate width of  $\approx 400$  ps. The maximum visibility of the central dip can be enhanced to 96.1%, because of the reduced accidental coincidence possibility. That visibility becomes 97.8% after subtracting the accidental coincidence counts. We note that, in the accidentals subtraction, the estimated double pairs are still included in the counts for the best estimate of the visibility. The single-photon counting rate remains constant during the measurement. However, here the background of the coincidence counting rate drops as the relative delay increases (see Supplementary Figure S6a). This drop is from the temporal overlap reduction for the gating of  $D_1$  and  $D_2$  at large relative delays of the HOM interferometer.

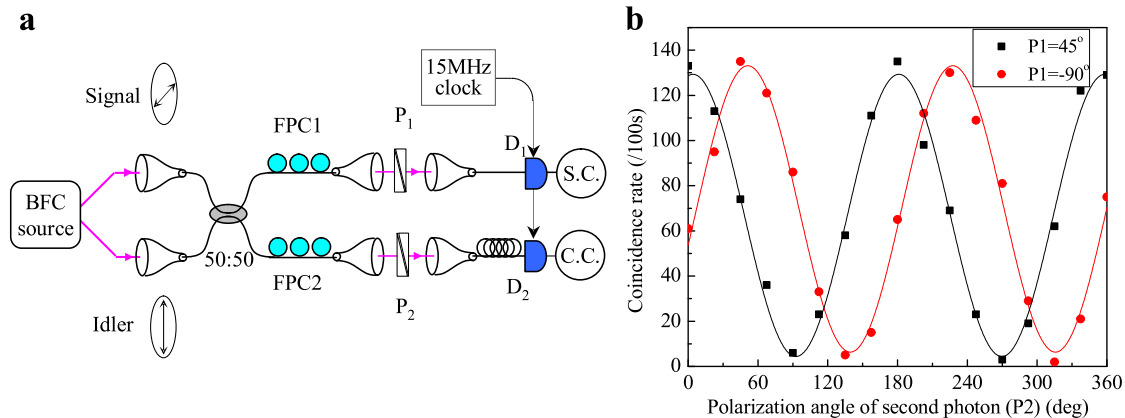


**Supplementary Figure S6 | HOM measurement with single-photon detectors with an effective gate width of  $\approx 400$  ps.** **a**, Coincidence and single counting rates as a function of the relative delay between the two arms of the HOM interferometer. The background of the coincidence counting rate drops because of the reduced overlap between the detection windows of  $D_1$  and  $D_2$ . **b**, Zoom-in coincidence and single counting rate around zero relative delay between the two arms. The visibility is measured to be 96.1 %, or 97.8 % after subtracting the accidental coincidence counts.

**VI. Polarization entanglement measurements of the high-dimensional biphoton frequency comb**

Before the hyperentanglement measurements, we test the polarization entanglement alone for the hyperentangled state. Supplementary Figure S7a shows the experiment setup. We mix the signal and idler photons on a 50:50 fiber coupler with orthogonal polarizations. By keeping the relative delay  $\delta\tau = 0$ , the signal and idler photons are well-overlapped temporally for the interference. We present a measurement for the polarization entanglement by measuring the coincidence counting rates while changing the angle of P2, when P1 was set at  $45^\circ$  and  $90^\circ$ , respectively. As shown in Supplementary Figure S7b, both results fit well with sinusoidal curves, with visibilities of  $91.2 \pm 1.6\%$  and  $93.0 \pm 1.3\%$ , which violate the Bell inequality by 12.8 and 17.7 standard deviations, respectively. This indicates the high-dimensional polarization

entangled state  $|\psi\rangle = \sum_{m=-N}^N |\omega_p/2 + m\Delta\Omega\rangle_1 |\omega_p/2 - m\Delta\Omega\rangle_2 \otimes (|H\rangle_1 |V\rangle_2 + |V\rangle_1 |H\rangle_2)$  is generated with high quality. Hence, in addition to the 4 frequency bits, the biphoton frequency comb also has polarization entanglement for use as a high-dimensional quantum communications platform.



**Supplementary Figure S7 | Polarization entanglement measurements of the high-dimensional biphoton frequency comb.** **a**, Illustrative experimental scheme. The signal and idler photons are sent to a 50:50 fiber coupler with orthogonal polarizations for the generation of polarization entanglement. P: polarizer; S.C.: single counts; C.C.: coincidence counts. **b**, Polarization entanglement measurements with P1 fixed at  $45^\circ$  and  $90^\circ$ . In both cases, we measured the coincidence counting rates at the two outputs while changing P2 from  $0^\circ$  to  $360^\circ$ . As shown by the black line (for  $P1 = 45^\circ$ ) and red line (for  $P1 = 90^\circ$ ), both measured results fit well with sinusoidal curves, with accidentals-subtracted visibilities of 91.2 % and 93.0 %, respectively.

## VII. High-dimensional hyperentanglement and Bell inequality statistics

We performed a series of hyperentangled measurements of the biphoton frequency comb with the visibilities summarized in Table 1 below, for the different P1 settings and different time-bin settings, across the energy-time basis and the polarization basis. The resulting standard deviation violation of the Bell inequality is computed correspondingly. Measurements are performed at 80-second integration times based on the tradeoff between the setup's long-term

stability over the complete hyperentanglement measurements and sufficiently reduced standard deviations of the coincidence counts. The Clauser-Horne-Shimony-Holt (CHSH)  $S$  parameter is determined from the polarization analysis angle set of the  $(|H\rangle|V\rangle + |V\rangle|H\rangle)$  triplet state:

$$S \equiv |-C(\pi/2, 7\pi/8) + C(\pi/4, 7\pi/8) + C(\pi/4, 5\pi/8) + C(\pi/2, 5\pi/8)| \quad (31)$$

**Table 1 | Visibilities for the interference fringes in the high-dimensional hyperentanglement measurement and Bell inequality violations.** “st.d.” denotes standard deviation  $\sigma$ .

		Time bin #0	Time bin #1	Time bin #2	Time bin #3	Time bin #4
P1 = 45°, Polarization basis	Visibility V	82.9%	80.1%	77.3%	73.8%	77.3%
	V (dark counts subtracted)	96.3%	96.2%	95.9%	93.8%	95.8%
	Bell violation (by st.d. $\sigma$ )	8.83	9.46	10.5	6.8	9.33
P1 = 45°, Energy-time basis	Visibility V	81.1%	74.1%	68.0%	60.0%	44.2%
	V (dark counts subtracted)	94.1%	87.5%	83.3%	74.7%	53.2%
	Bell violation (by st.d. $\sigma$ )	7.34	5.19	4.83	2.12	none
P1 = 90°, Polarization basis	Visibility V	81.4%	76.6%	75.8%	75.1%	75.3%
	V (dark counts subtracted)	96.9%	95.0%	95.8%	94.5%	95.7%
	Bell violation (by st.d. $\sigma$ )	10.95	8.09	7.62	8.51	7.97
P1 = 90°, Energy-time basis	Visibility V	80.3%	72.3%	67.5%	59.4%	44.2%
	V (dark counts subtracted)	95.9%	89.0%	84.3%	73.6%	54.1%
	Bell violation (by st.d. $\sigma$ )	7.87	8.34	5.67	1.92	none
CHSH $S$ parameter		2.71	2.67	2.76	2.74	2.53